

All-optical reconfiguration of far-field singularities in a photonic-crystal laser

Abhishek Padhy,^{1,2} Zhiyi Yuan,^{3,4} Mohammed Hamdad,¹ Panagiotis Nianios,¹ Romane Houvenaghel,¹ Aziz Benamrouche,¹ Nicolas Roy,² Thanh Phong Vo,¹ Christian Seassal,¹ Xavier Letartre,¹ Lotfi Berguiga,¹ Michaël Lobet,² Ségolène Callard,¹ and Hai Son Nguyen^{1,4,5,*}

¹*Ecole Centrale de Lyon, CNRS, INSA Lyon, Université Claude Bernard Lyon 1, CPE Lyon, Institut des Nanotechnologies de Lyon (INL), UMR 5270, 69130 Écully, France*

²*Department of Physics, NISM Institute, University of Namur, Rue de Bruxelles 61, 5000 Namur, Belgium*

³*Centre for OptoElectronics and Biophotonics (COEB),*

School of Electrical and Electronic Engineering, Nanyang Technological University, Singapore 639798

⁴*CNRS-International-NTU-Thales Research Alliance (CINTRA), IRL 3288, Singapore*

⁵*Institut Universitaire de France (IUF), France*

(Dated: March 10, 2026)

Singular optics has emerged as an important research area with diverse applications, yet controlling optical singularities in nanophotonic emitters is typically limited by fixed subwavelength geometries and diffraction-limited control. Here, we circumvent this limitation and demonstrate an all-optical mechanism for reconfiguring far-field singularities in a photonic crystal laser. The underlying principle involves optical pumping, which creates a mesoscopic potential landscape whose spatial variations are slow compared to the lattice period. Such a potential localizes a Bloch band into trapped states whose envelope functions, and thus far-field singularity textures, are defined by the pump geometry. Using a honeycomb photonic crystal that supports a symmetry-protected bound state in the continuum, we achieve room-temperature telecom-band lasing with real-space polarisation singularities that are pinned at the extrema of the envelope function and can be reconfigured in both number and position by shaping the pump, while the intrinsic momentum-space singularity at the Γ point remains preserved. The experimental observations align quantitatively with an analytical framework that combines the Bloch mode of the structure and envelope function theory, establishing envelope engineering as a versatile route to programmable singular-light emission in active photonic lattices.

Optical singularities, points where the phase or polarization of light is undefined, play a central role in structured-light physics and carry quantized topological charges [1, 2]. Their control underpins applications in robust communication [3, 4], precision metrology [5], and vortex lasing [6–9]. In nanophotonics, such singularities may be imposed externally through phase engineering or arise intrinsically from the eigenmodes of resonant metasurfaces and photonic crystals (PhCs). Bound states in the continuum (BICs), whose radiation vanishes by symmetry or interference, provide a powerful route to generating singular beams directly from photonic resonances [7, 10–12].

Achieving dynamic control of these singularities remains challenging because the far-field texture of a Bloch mode is fixed by the unit-cell geometry, and conventional structures offer little reconfigurability. Thermal tuning in phase-change PhCs allows switching between BIC lasing modes with different topological charges [13], and photoisomerization in organic PhCs provides a similar mode-switching mechanism [14], but neither approach can reshape the singularity texture of a given Bloch resonance. Recent optical-control schemes modulate refractive index at the unit-cell scale: ultrafast pumping can destroy BIC singularities by breaking in-plane symmetries

[8], and gain-loss perturbations suppress vortex emission [9, 15]. Sub-unit-cell pumping can even alter the response of individual elements [16], but remains limited to passive linewidth tuning and does not enable continuous control of far-field singularities. Fundamentally, all these schemes attempt to reconfigure the unit cell, an operation constrained by the diffraction limit. In this work, we introduce an alternative approach, instead of modifying the subwavelength Bloch function, we reconfigure the mesoscopic envelope of a PhC resonance using optical pumping (see Fig. 1). Carrier injection creates a smooth in-plane potential that localizes a Bloch band into trapped states whose envelope functions obey a two-dimensional Schrödinger equation, which can be shaped arbitrarily by the pump profile. Because the radiated field is the product of the Bloch-mode far field and its envelope, this mechanism enables reconfigurable far-field singularities without altering the photonic crystal itself.

As a proof of concept, we use a honeycomb PhC supporting the lowest-energy band with isotropic negative-mass dispersion and a monopolar BIC at the Γ -point ($\mathbf{k}_{\parallel} = \mathbf{0}$). Optical pumping forms tunable potentials that trap this band and yield lasing trapped states whose real-space far-field polarization singularities are pinned at the extrema of the envelope function and can be programmed by the pump geometry, whereas the momentum-space singularity remains fixed. Lasing occurs at room temperature and telecom wavelengths, and the measurements

* hai-son.nguyen@ec-lyon.fr

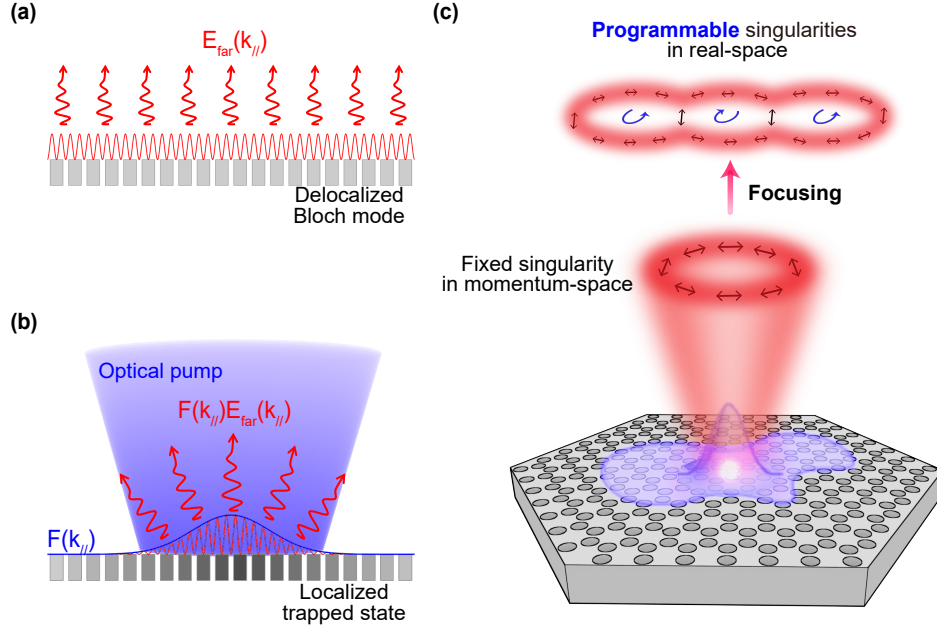


Figure 1. **Concept:** (a) In the absence of pumping, a Bloch resonance of a PhC slab is delocalized over the lattice and radiates into the continuum with a fixed momentum-space far-field pattern $\mathbf{E}_{\text{far}}(\mathbf{k}_{\parallel})$. (b) A shaped optical pump injects carriers and creates a smooth in-plane potential that localizes the Bloch band into a trapped state with envelope $F(\mathbf{r}_{\parallel})$. In momentum space, the trapped-state emission inherits the Bloch-mode topology but is modulated by the envelope spectrum, $\mathbf{E}_{\text{far}}^{\text{trap}}(\mathbf{k}_{\parallel}) \propto F(\mathbf{k}_{\parallel})\mathbf{E}_{\text{far}}(\mathbf{k}_{\parallel})$. (c) Schematic of the all-optical control of the photonic crystal laser with singularities. The far-field singularities in the real-space can be controlled by the optical pump.

agree quantitatively with envelope-function theory, establishing a general route to reconfigure singular beams in active photonic lattices.

RESULTS

Theoretical framework

We first consider the generic guided resonances of a PhC slab in the absence of optical pumping. For a fixed in-plane wave vector $\mathbf{k}_{\parallel} = (k_x, k_y)$, the corresponding Bloch mode inside the slab can be expanded over a finite basis consisting of guided modes $\{|n\rangle\}$ of an effective homogeneous slab, each carrying a reciprocal lattice vector \mathbf{G}_n . The guided modes in the basis share the same out-of-plane profile $u(z)$ and differ only in their in-plane Bloch harmonics. Factoring out the global Bloch phase $e^{i\mathbf{k}_{\parallel} \cdot \mathbf{r}_{\parallel}}$ for compactness, the near field can be written as $\mathbf{E}_{\text{near}, \mathbf{k}_{\parallel}}(\mathbf{r}_{\parallel}, z) = u(z) \sum_n A_n(\mathbf{k}_{\parallel}) e^{i\mathbf{G}_n \cdot \mathbf{r}_{\parallel}} \mathbf{p}_n$, where $\mathbf{r}_{\parallel} = (x, y)$ denotes the in-plane coordinate, $\{\mathbf{p}_n\}$ are the polarization vectors of the guided-mode basis. Here, $A_n(\mathbf{k}_{\parallel})$ are the expansion coefficients obtained by diagonalizing the effective non-Hermitian Hamiltonian of the PhC slab [17]. Radiation into the continuum is obtained by projecting this Bloch mode onto the outgoing Fabry-Pérot channel of the unpatterned slab (Fig. 1(a)). In the single-channel regime relevant here (subwavelength

lattice, thus the zeroth diffraction order inside the light cone is the only leaky channel), the radiated field in direction \mathbf{k}_{\parallel} is proportional to the same guided-mode coefficients, but without the fast lattice harmonics $e^{i\mathbf{G}_n \cdot \mathbf{r}_{\parallel}}$ [17]: $\mathbf{E}_{\text{far}}(\mathbf{k}_{\parallel}) \propto \sum_n \sqrt{\gamma_n} A_n(\mathbf{k}_{\parallel}) \mathbf{p}_n$ where γ_n is the radiative loss rate of the guided mode $|n\rangle$ when folded inside the light cone and coupled to the radiative continuum. The polarization texture and the existence of BICs are encoded in this farfield vector, and the radiative rate $\gamma(\mathbf{k}_{\parallel})$ of the resonance is given by the emitted intensity $|\mathbf{E}_{\text{far}}|^2$.

The complex eigenfrequency of the guided resonance can be described as $\omega(\mathbf{k}_{\parallel}) \simeq \omega_0 + \frac{\hbar|\mathbf{k}_{\parallel}|^2}{2m} - i\gamma(\mathbf{k}_{\parallel})$, where m is the effective mass of the Bloch resonance. In general, the photonic band can exhibit anisotropy, but here, the guided resonances have been chosen such that the effective mass m is negative and isotropic. Under optical pumping, photogenerated carriers produce a carrier-induced optical nonlinearity that leads to a spatially varying refractive-index change $\Delta n(\mathbf{r}_{\parallel}) < 0$ [18]. This smooth index decrease maps onto an effective in-plane blueshift potential $V(\mathbf{r}_{\parallel})$ for the Bloch band [19, 20], thereby trapping the lowest-energy states in a pump-defined landscape. Within the effective-mass approximation, considering a smooth varying potential $V(\mathbf{r}_{\parallel})$ and neglecting losses in the in-plane eigenproblem for small $\gamma(\mathbf{k}_{\parallel})$, the in-plane dynamics are governed by a standard Hermitian Schrödinger equation for the envelope function

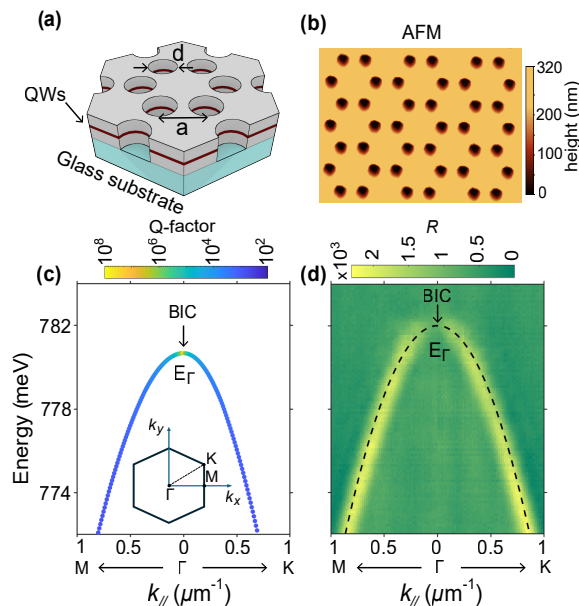


Figure 2. **The fabricated photonic crystal device and its dispersion:** (a) Schematic of the fabricated honeycomb PhC slab. The lattice has a period $\Lambda = a\sqrt{3}$ with lattice constant $a = 445$ nm, hole diameter $d = 335$ nm, and total membrane thickness $t = 240$ nm. (b) Atomic-force-microscopy (AFM) image of the fabricated surface. (c) Numerically computed band structure using Legume, showing the lowest-energy band that hosts a monopolar symmetry-protected BIC at the Γ -point. The band is nearly isotropic and displays a negative effective mass. (d) Experimental angle-resolved photoluminescence along the Γ -K and Γ -M directions, exhibiting the vanishing radiative loss at Γ which is characteristic of the BIC. The dashed line represents a parabolic fit to the measured dispersion.

$F(\mathbf{r}_{\parallel})$ [21]: $-\frac{\hbar^2}{2m} \nabla_{\mathbf{r}_{\parallel}}^2 F(\mathbf{r}_{\parallel}) + V(\mathbf{r}_{\parallel}) F(\mathbf{r}_{\parallel}) = E F(\mathbf{r}_{\parallel})$. Because $m < 0$, a positive potential $V(\mathbf{r}_{\parallel})$ has a confining effect and localizes light under the pump spot, forming trapped states. Each trapped state corresponds to a solution $F(\mathbf{r}_{\parallel})$ of the Schrödinger equation given above; its Fourier transform $F(\mathbf{k}_{\parallel}) = \text{FT}[F(\mathbf{r}_{\parallel})]$ specifies how the Bloch resonances are superposed in momentum space. The near field of a trapped state can thus be written as a superposition of Bloch modes weighted by $F(\mathbf{k}_{\parallel})$:

$$\mathbf{E}_{\text{near}}^{\text{trap}}(\mathbf{r}_{\parallel}) = \sum_{\mathbf{k}_{\parallel}} F(\mathbf{k}_{\parallel}) \mathbf{E}_{\text{near}, \mathbf{k}_{\parallel}}(\mathbf{r}_{\parallel}, z), \quad (1)$$

or, in the continuum limit, as an integral over \mathbf{k}_{\parallel} . The corresponding far field of the trapped state in momentum space is

$$\mathbf{E}_{\text{far}}^{\text{trap}}(\mathbf{k}_{\parallel}) = F(\mathbf{k}_{\parallel}) \mathbf{E}_{\text{far}}(\mathbf{k}_{\parallel}), \quad (2)$$

that is, the original Bloch far-field pattern is modulated by the envelope spectrum $F(\mathbf{k}_{\parallel})$ [see Fig. 1(b)]. Finally, the far field of the trapped state in real space is obtained

by the inverse Fourier transform of Eq. (2) as follows:

$$\mathbf{E}_{\text{far}}^{\text{trap}}(\mathbf{r}_{\parallel}) = \text{FT}^{-1}[F(\mathbf{k}_{\parallel}) \mathbf{E}_{\text{far}}(\mathbf{k}_{\parallel})]. \quad (3)$$

Equations (1)–(3) make the central mechanism explicit: the singularities of the radiated field are dictated jointly by the Bloch resonance, through $\mathbf{E}_{\text{far}}(\mathbf{k}_{\parallel})$, and by the pump-induced envelope, through $F(\mathbf{k}_{\parallel})$. The Bloch contribution determines the intrinsic momentum-space topology carried by the underlying band, whereas the envelope reshapes the distribution of momenta and thereby controls the number, position, and structure of the singularities in the real space.

A special case arises when the underlying Bloch resonance is a symmetry-protected BIC. Since such modes satisfy $\mathbf{E}_{\text{far}}(\mathbf{k}_{\parallel} = 0) = \mathbf{0}$, Eq. (2) ensures that any trapped state constructed from them also obeys $\mathbf{E}_{\text{far}}^{\text{trap}}(\mathbf{k}_{\parallel} = 0) = \mathbf{0}$, independently of the envelope function. The momentum-space singularity at the Γ point is therefore preserved under arbitrary optical pumping. In contrast, the real-space far field directly reflects the envelope of the trapped state. For symmetry-protected BICs of winding number $+1$, commonly encountered in photonic crystal slabs with C_4 or C_6 symmetry, the Bloch radiation scales as $\mathbf{E}_{\text{far}}(\mathbf{k}_{\parallel}) \propto |\mathbf{k}_{\parallel}| \mathbf{u}_{\varphi}$. Consequently, the radiation spectrum of a trapped state with envelope $F(\mathbf{k}_{\parallel})$ becomes $|\mathbf{k}_{\parallel}| F(\mathbf{k}_{\parallel}) \mathbf{u}_{\varphi}$. According to Eq. 3, the corresponding real-space far field is therefore given by the inverse Fourier transform, leading to:

$$\mathbf{E}_{\text{far}}^{\text{trap}}(\mathbf{r}_{\parallel}) \propto \hat{\mathbf{z}} \times \nabla F(\mathbf{r}_{\parallel}). \quad (4)$$

Equation (4) shows that the real-space far field is governed entirely by the spatial variation of the envelope function $F(\mathbf{r}_{\parallel})$. In particular, polarization singularities of $\mathbf{E}_{\text{far}}^{\text{trap}}(\mathbf{r}_{\parallel})$ occur at points where $\nabla F(\mathbf{r}_{\parallel}) = 0$, corresponding to extrema of the envelope. These results reveal a clear separation between momentum-space topology and real-space structure: the Bloch resonance fixes the polarization vortex at Γ in \mathbf{k}_{\parallel} -space, whereas the pump-defined envelope determines the number, position, and spatial distribution of polarization singularities in real space.

Proof of Concept

To demonstrate envelope-function control experimentally, we use a two-dimensional honeycomb photonic crystal slab patterned into an InP/InAsP/InP multiple-quantum-well membrane [Fig. 2(a–b)]. The heterostructure is grown by molecular beam epitaxy, the active InP-based membrane is molecularly bonded onto a glass substrate, and the PhC is defined by electron-beam lithography followed by reactive-ion etching.

Numerical band-structure calculations were performed using the guided-mode-expansion solver Legume [22], to-

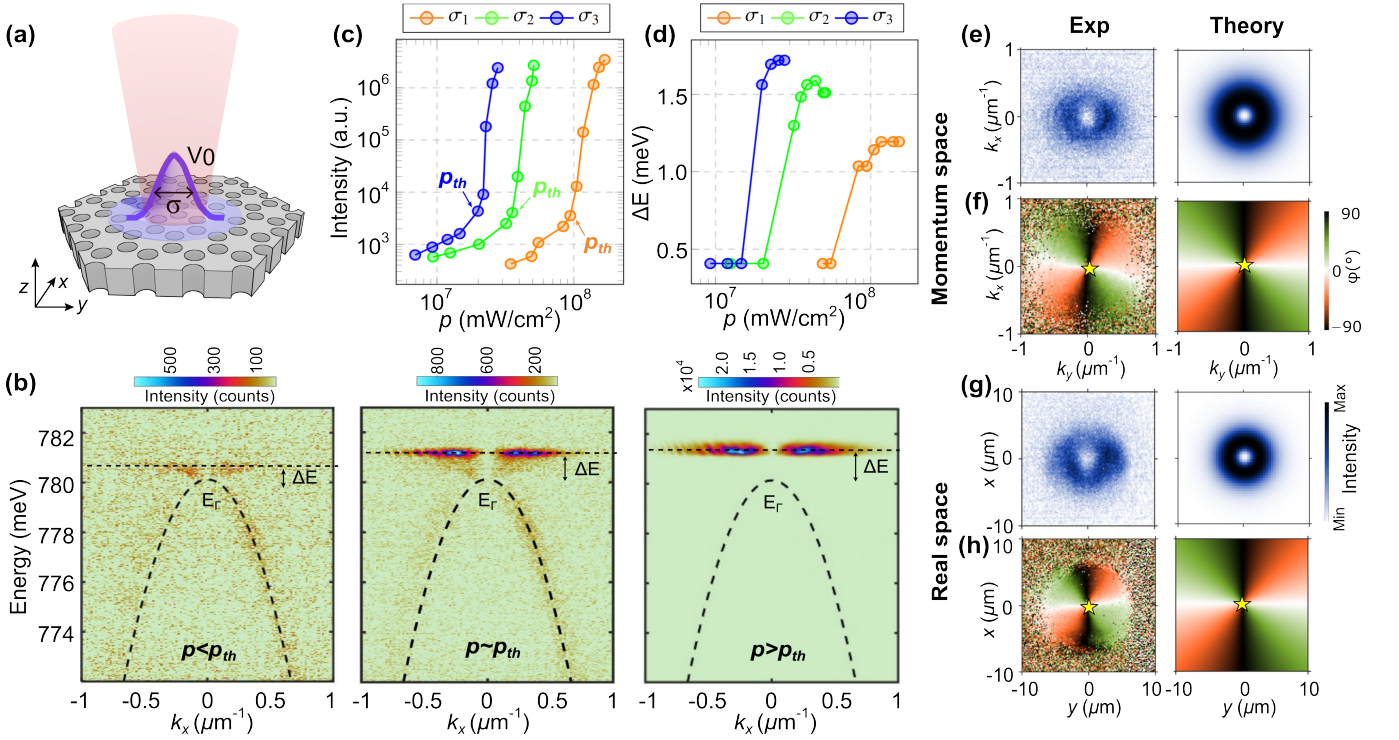


Figure 3. **Lasing characterization and farfield measurements for single pump spot:** (a) Schematic of single spot pumping on the PhC with spot size σ . The pump creates a potential $V(\mathbf{r}_{\parallel})$, which induces a trapped-state envelope function $F(\mathbf{r}_{\parallel})$. (b) Experimental energy-momentum dispersion along k_x below ($p < p_{th}$), around ($p \sim p_{th}$) and above threshold ($p > p_{th}$) pump power density (p) for spot waist $\sigma_1 = 3.2 \mu\text{m}$. The fundamental mode is fitted with a parabola with $\alpha = -13.4 \text{ meV} \cdot \mu\text{m}^2$, and the confinement energy (ΔE) is the difference between the trapped mode energy and energy at Γ -point (E_r). (c) Total integrated trapped-state intensity vs pump power density p for three pump waists $\sigma_1 = 3.2 \mu\text{m}$, $\sigma_2 = 7.1 \mu\text{m}$, $\sigma_3 = 11.1 \mu\text{m}$. (d) Confinement energy ΔE vs pump power for the three spot waists. (e–h) Far-field characterization of the trapped state above threshold for $\sigma = 3.2 \mu\text{m}$. Panels show (left) experimental momentum-space and real-space intensity and polarization textures and (right) corresponding analytical predictions from the envelope-function model. The yellow stars mark the polarization singularities. The theoretical results were calculated with the parameter $V_0 = 4.8 \text{ meV}$. [Refer Ext. Fig. A1 for the polarization resolved farfield lasing images and Ext. Fig. A5 for farfield results computed via FDTD.]

gether with angle-resolved photoluminescence measurements [Fig. 2(c-d)](see Methods for setup details). They show that the lowest-energy band (monopolar band) of the fabricated honeycomb PhC is nearly isotropic and follows a parabolic dispersion with negative effective mass. At the Γ -point, this band hosts a symmetry-protected monopolar BIC, evidenced by the vanishing radiative loss $\gamma(\mathbf{k}_{\parallel}) \propto |\mathbf{k}_{\parallel}|^2$. A full analytical description of this Bloch resonance, including the effective non-Hermitian Hamiltonian and its eigenmodes, is provided in Methods. In the following, we use this monopolar band to engineer the trapped states, whose envelope function is entirely shaped by the optical pump. However, we note that Equations (2)–(3), which factorize the trapped-state radiation as $\mathbf{E}_{\text{far}}^{\text{trap}}(\mathbf{k}_{\parallel}) = F(\mathbf{k}_{\parallel})\mathbf{E}_{\text{far}}(\mathbf{k}_{\parallel})$, are quantitatively accurate only when the target Bloch band is well isolated from other leaky bands over the momentum range sampled by $F(\mathbf{k}_{\parallel})$, so that interband mixing can be neglected. This condition is well satisfied for the monopolar band studied here: it is spectrally isolated around Γ , and

its closest neighbor is the hexapolar band, which is itself (near Γ) a BIC band. For trapped states based on the hexapolar band, the situation is more subtle. First, the hexapolar BIC is second order (winding number 2), so its intrinsic radiative loss scales as $\gamma \propto |\mathbf{k}_{\parallel}|^4$ (instead of $\propto |\mathbf{k}_{\parallel}|^2$ for the monopolar case), making its own radiation extremely weak and therefore more sensitive to residual admixture from other radiating bands even when the hexapolar band is spectrally separated. Second, two nearly degenerate dipolar modes that are leaky (non-BIC) lie in the vicinity; their hybridization with the hexapolar trapped state can induce a finite linewidth already at $\mathbf{k}_{\parallel} = \mathbf{0}$ through the dipolar leakage channels. (See Supplemental Material for a detailed discussion.)

The sample was excited using a femtosecond laser at 800 nm, shaped by a spatial light modulator (SLM). The pump was focused on a single Gaussian spot on the PhC slab [Fig. 3(a)], injecting carriers into the InP/InAsP/InP multiple-quantum-well membrane and creating a smooth negative variation of refractive-index

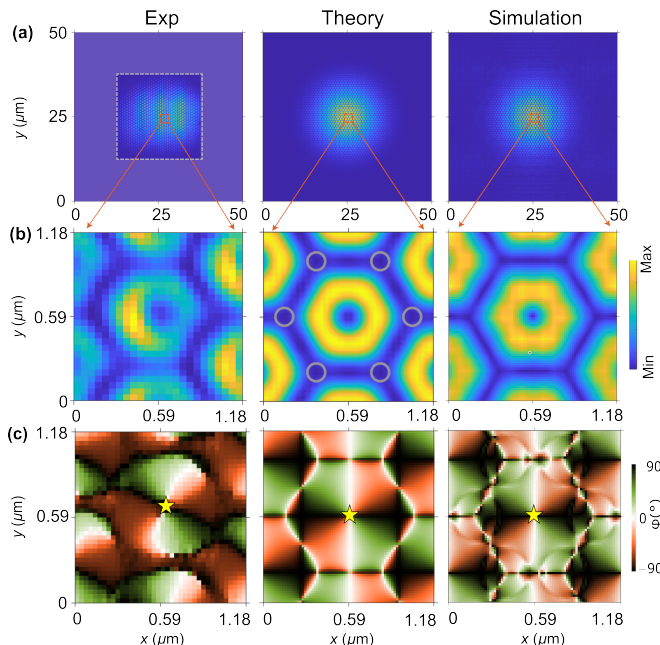


Figure 4. **Nearfield maps for single pump:** (a) Large-area SNOM (left panel), analytical model (middle), and FDTD numerical (right) of near-field map of the trapped state under a single Gaussian pump. The white dashed line box represents the measurement region. (b) Zoomed-in near-field amplitude showing the fast spatial oscillations of the Bloch resonance on the scale of the photonic crystal lattice. (c) Polarization-resolved mapping of the in-plane electric field.

that acts as a confining potential for the lowest-energy Bloch band. This potential can be modeled as $V(\mathbf{r}_{\parallel}) = V_0 e^{-|\mathbf{r}_{\parallel}|^2/\sigma^2}$, where the depth V_0 is set by the injected carrier density, and the trap size σ is controlled precisely by the SLM.

Figure 3(b) shows the measured dispersion with increasing pump power density. At low pump power density, the emission follows the unperturbed band with inverted parabolic dispersion $E(k_x) = E_{\Gamma} + \alpha k_x^2$; a fit gives $\alpha = -13.4 \text{ meV } \mu\text{m}^2$, confirming the negative effective mass. Upon increasing the pump power, a dispersionless line appears above E_{Γ} , indicating the formation of a trapped state with confinement energy ΔE . Below threshold, the trapped mode blueshift increases with pump power as injected carriers deepen the effective confining potential [Fig. 3(c)]. Above threshold, the blueshift saturates as stimulated emission clamps the carrier density. Additional pump power, therefore, produces photons rather than increasing the carrier reservoir, fixing the confinement depth $\approx 4.8 \text{ meV}$ (see Methods).

The total flatband intensity showed a characteristic S -shaped dependence on the pump power density, demonstrating single-mode lasing. Notably, the lasing threshold decreases when the pump-spot size increases [$\sigma_1 < \sigma_2 < \sigma_3$ in Fig. 3(c)]. A smaller excitation spot produces a broader momentum-space envelope, leading to stronger

overlap with the high- k components of the Bloch mode, whose radiative losses scale as $|\mathbf{k}_{\parallel}|^2$. The trapped-state radiative loss therefore scales approximately as $1/\sigma^2$. Consequently, smaller traps require a higher carrier density at threshold, whereas larger traps exhibit weaker loss and lase at lower gain. The saturated confinement energy ΔE above the threshold also increases with the pump-spot diameter [Fig. 3(d)]. Indeed, a larger σ creates a broader and shallower potential, and in the negative-mass Schrödinger model, the trapped-state energy shifts upward.

We investigate the far-field radiation pattern for $\sigma = 3.2 \mu\text{m}$ by examining the corresponding far-field intensity and polarization textures in both momentum and real space above threshold. The measurements, together with the analytical predictions of the envelope-function model, are shown in Fig. 3(e-h). The radiation patterns remain unchanged for other spot sizes. The momentum-space lasing emission exhibits a polarization vortex centered at $\mathbf{k}_{\parallel} = \mathbf{0}$ [Fig. 3(e-f)], characteristic of the monopolar BIC of the underlying Bloch mode [17]. As follows from Eq. (2), the radiative amplitude vanishes at the Γ -point irrespective of the envelope function. The momentum-space singularity is therefore preserved independently of the pump profile. In real space, however, the far-field pattern is dictated by the envelope of the trapped state. According to Eq. (4), the emitted field is proportional to the spatial gradient of the envelope function. For a radially symmetric envelope $F(\mathbf{r}_{\parallel}) = F(|\mathbf{r}_{\parallel}|)$ produced by a symmetric pump spot, the far field reduces to $F'(|\mathbf{r}_{\parallel}|) \mathbf{u}_{\varphi}$. In the case of the Gaussian pump used here, this results in a donut-shaped real-space intensity distribution with a single polarization singularity at the center, in agreement with the measurements shown in Fig. 3(g-h).

Near-field imaging with scanning near-field optical microscopy (SNOM) [23, 24] provides direct access to both the mesoscopic envelope and the microscopic Bloch component of the trapped state. The large-area SNOM map in Fig. 4(a) reveals a Gaussian-like intensity profile localized beneath the pump, with a maximum at the pump center and a smooth decay, in agreement with the confined state predicted by the effective-mass model. The slight elongation of the envelope is likely caused by a weak ellipticity of the excitation focus in the SNOM setup. Zoomed-in views [Figs. 4(b-c)] resolve the rapid subwavelength oscillations associated with the Bloch mode. Within each unit cell, the measured near field displays the characteristic azimuthal rotation expected for the magnetic-monopole resonance: the in-plane field winds around the hexagon center with a full 2π phase rotation. Polarization-resolved SNOM measurements [Fig. 4(c)] further corroborate this picture, showing a clear vortex-like winding of the local electric-field vector. Together, these results demonstrate that the trapped state preserves the microscopic polarization texture of the monopolar Bloch resonance

while acquiring a mesoscopic envelope dictated by the optically induced potential. The SNOM observations are in excellent agreement with both the analytical envelope-function model and full-wave finite-difference time-domain (FDTD) simulations. In the FDTD calculations, we emulate the optically induced potential by introducing a Gaussian refractive-index perturbation, $n(\mathbf{r}_{\parallel}) = n_0 + \delta_n \exp(-|\mathbf{r}_{\parallel}|^2/\sigma^2)$, with $n_0 = 3.162$ and $\delta_n = -0.022$.

Reconfigurable singularities

As shown by Eq. (4), polarization singularities occur at points where $\nabla F(\mathbf{r}_{\parallel}) = 0$, i.e., at extrema of the envelope function. This relation provides a direct route to engineer the spatial distribution of singularities by shaping the pump-defined envelope. To illustrate this principle, we patterned the pump into two Gaussian spots separated by a distance L , forming a diatomic photonic “molecule” [Fig. 5(a)]. Each pump spot defines an optically induced trap that plays the role of an “atom,” while their overlap enables tunnel-like coupling controlled by L . The pump waist was fixed to $\sigma = 3.25 \mu\text{m}$, and the device was driven above threshold into the lasing regime.

The measured energy–momentum dispersions for decreasing L are shown in Fig. 5(b). For large separations (top row), only a single trapped-state branch is visible, corresponding to two nearly independent localized states. As L decreases, coupling between the traps increases and the lasing mode splits into anti-bonding (AB) and bonding (B) branches, analogous to the molecular eigenstates of a double-well potential [25]. The dependence of their energies on L is plotted in Fig. 5(c) and agrees quantitatively with the effective-mass Schrödinger model for a two-well potential $V(x, y) = V_0 \left[e^{((x-L/2)^2 - y^2)/\sigma^2} + e^{-((x+L/2)^2 + y^2)/\sigma^2} \right]$, using V_0 obtained from the method discussed for a single spot. This establishes that the lasing branches correspond to the B and AB envelope eigenstates of pump-induced potential landscape.

Because the underlying Bloch resonance is a monopolar BIC with $\mathbf{E}_{\text{far}}(\mathbf{0}) = \mathbf{0}$, both B and AB modes retain a single polarization vortex pinned at the Γ point, as seen in the momentum-space measurements of Fig. 5(d–e). In real space, however, the two modes exhibit strikingly different polarization singularity structures. This difference follows directly from the extrema of their envelope functions. The antibonding mode possesses two extrema—one maximum and one minimum localized at the two pump spots—while the bonding mode exhibits three extrema: two maxima at the pump positions and one minimum at the center of the molecule. According to Eq. (4), these extrema correspond to points where $\nabla F(\mathbf{r}_{\parallel}) = 0$, and therefore to polarization singularities

in the emitted field. Consistently, the AB mode displays two singularities associated with the two extrema of its envelope, whereas the B mode exhibits three singularities, reflecting its three extrema [Fig. 5(f–g)]. The analytical far-field patterns evaluated from the envelope-function model [right column of Fig. 5(d–e)] reproduce the measured vortex configurations with no adjustable parameters. These results demonstrate that while the monopolar BIC fixes the topology in momentum space, the pump-defined envelope determines the spatial distribution of polarization singularities in real space.

To demonstrate the scalability of envelope-function control, we also investigated a configuration using three identical pump spots arranged linearly with equal separation $L = 13 \mu\text{m}$. The three pump spots generate a composite potential consisting of three overlapping Gaussian wells, which supports three trapped eigenstates—the photonic analogue of the three molecular orbitals in a linear triatomic chain. These states appear as three distinct lasing modes and correspond to the three lowest solutions of the effective-mass Schrödinger equation for a triple-well potential. Extended Figure A3 compares the experimental and theoretical far-field emission patterns of the three trapped modes in both real space and momentum space, together with the associated polarization textures obtained from polarization-resolved tomography. As expected, all three modes preserve the same momentum-space vortex at Γ , inherited from the monopolar BIC of the underlying Bloch resonance. In contrast, each trapped mode exhibits a distinct real-space polarization-singularity pattern determined by the nodal structure of its envelope function: the ground state (Mode 1) displays one singularity, the first excited state (Mode 2) displays two singularities, and the second excited state (Mode 3) displays three singularities. The experimental maps and analytical predictions show excellent quantitative agreement in both intensity and polarization textures, including the singularity locations indicated by the yellow stars in Extended Fig. A3.

These results demonstrate that envelope-function engineering enables reconfigurable real-space singularities—including their number, type, and position—while the momentum-space topology remains protected by the symmetry of the underlying Bloch mode. Adjusting the pump separation L continuously tunes the molecular hybridization and therefore the far-field vortex pattern. More broadly, because the effective potential is written optically, the approach naturally extends to more complex pump geometries (e.g., multi-spot arrays, asymmetric patterns, and dynamically modulated profiles), providing additional degrees of freedom to sculpt the trapped-state landscape and the resulting singularity textures on demand. This concept thus offers a scalable route to programmable singular-beam generation in active photonic crystals.

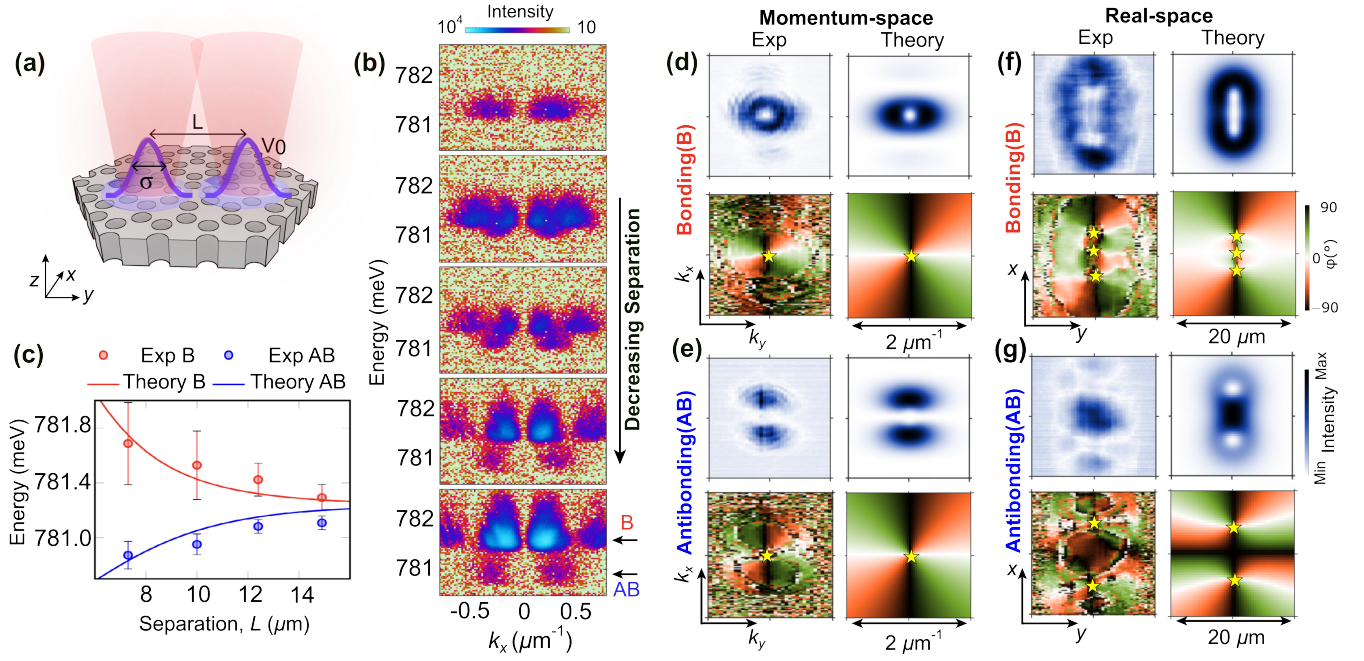


Figure 5. **Two-spot pumping and the demonstration of reconfigurable singularities in the farfield:**(a) Schematic of two trapped states induced by a double pump spot with varying separation distance L with fixed spot waist $\sigma = 3.25\mu\text{m}$. (b) Energy-momentum dispersion along k_x for various L (14.9, 11.9, 10.4, $7.2\mu\text{m}$), decreasing from top panel ($14.9\mu\text{m}$) to the bottom panel ($7.2\mu\text{m}$). Far-field patterns (for $L=7.2\mu\text{m}$) in momentum and real space for both Bonding (d) and Anti-bonding (e) modes, and the experimental results (left) are supported by the analytical/theory results (right). Singularities are denoted by yellow stars. The theoretical results are calculated with parameter $V_0 = 4.6\text{ meV}$. [Refer to Ext. Fig. A2 for the corresponding polarization resolved farfield lasing images and Ext. Fig. A5 for farfield results computed via FDTD.]

CONCLUSION

We demonstrated an all-optical mechanism for reconfiguring far-field singularities in active photonic crystals by tailoring the mesoscopic envelope of a Bloch resonance. This approach bypasses the need to modify subwavelength unit-cell geometries and instead uses pump-induced carrier potentials to localize a Bloch band into trapped states described by a two-dimensional Schrödinger equation. In a honeycomb PhC supporting a monopolar BIC, we demonstrated that the intrinsic momentum-space singularity remains fixed, whereas the real-space polarization texture can be continuously reshaped through the envelope function. Multi-spot pumping enables trapped states hosting controllable numbers and positions of singularities, which is in quantitative agreement with the analytical theory. Because the mechanism relies solely on carrier injection, reconfiguration can, in principle, operate on picosecond timescales [19, 20, 26, 27]. Extensions toward dynamic pump modulation and programmable multi-spot pumping could enable reconfigurable tight-binding Hamiltonians for quantum simulation [28, 29] and laser-array architectures with controllable coupling for neuromorphic computing [30, 31], further expanding the possibilities of ultra-

fast programmable structured-light emitters.

ACKNOWLEDGEMENTS

We thank Philippe Regreny for growing epitaxial structures. Wafer bonding technology was supplied by CEA-LETI. This work was supported by the French National Research Agency (ANR) under the projects NANOEC (ANR07-NANO-036), POLAROID (ANR-24-CE24-7616-01), and SUPER-HERO (ANR-25-CE24-4066). A.P. was supported by the LABEX iMUST of the University of Lyon through the “Stage d’Innovation 2023–24” program. M.L. is a Research Associates of the Fonds de la Recherche Scientifique—FNRS. Computational resources have been provided by the Consortium des Equipements de Calcul Intensif (CECI), funded by the Fonds de la Recherche Scientifique de Belgique (F.R.S.-FNRS) under Grant No. 2.5020.11 and by the Walloon Region. The present research also benefited from computational resources made available on Lucia, the Tier-1 supercomputer of the Walloon Region, infrastructure funded by the Walloon Region under the grant agreement n°1910247. A.P. dedicates this work to N. Palo and M. Palo.

AUTHOR CONTRIBUTIONS

H.S.N. conceived the idea and developed the theoretical model. S.C., T.P.V., and C.S. fabricated the structures. A.B. and S.C. carried out the near-field (SNOM) measurements. Z.Y., X.L., and N.R. performed the FDTD simulations. L.B. and A.P. contributed to the optical-bench setup and SLM characterization. A.P., H.S.N., P.N, M.H. and R.H. performed the far-field optical measurements and analyzed the experimental data in comparison with theory. H.S.N., Z.Y., S.C., M.L., and A.P. wrote the initial draft of the manuscript. All authors reviewed, edited, and approved the final version.

COMPETING INTERESTS

The authors declare no conflicts of interest.

-
- [1] Y. Shen, X. Wang, Z. Xie, C. Min, X. Fu, Q. Liu, M. Gong, and X. Yuan, *Light: Science & Applications* **8**, 90 (2019).
- [2] M. S. Soskin, S. V. Boriskina, Y. Chong, M. R. Dennis, and A. Desyatnikov, *Journal of Optics* **19**, 010401 (2017).
- [3] A. E. Willner, H. Huang, Y. Yan, Y. Ren, N. Ahmed, G. Xie, C. Bao, L. Li, Y. Cao, Z. Zhao, J. Wang, M. P. J. Lavery, M. Tur, S. Ramachandran, A. F. Molisch, N. Ashrafi, and S. Ashrafi, *Advances in Optics and Photonics* **7**, 66 (2015).
- [4] B. Ndagano, I. Nape, M. A. Cox, C. Rosales-Guzmán, and A. Forbes, *Journal of Lightwave Technology* **36**, 292 (2018).
- [5] M. Cheng, W. Jiang, L. Guo, J. Li, and A. Forbes, *Light: Science & Applications* **14**, 4 (2025).
- [6] M. Hwang, H. Kim, J. Kim, B. Yang, Y. Kivshar, and H. Park, *Nature Photonics* **18**, 286 (2023).
- [7] R. Mermet-Lyauodoz, C. Symonds, F. Berry, E. Drouard, C. Chevalier, G. Trippé-Allard, E. Deleporte, J. Bellessa, C. Seassal, and H. S. Nguyen, *Nano Letters* **23**, 4152 (2023).
- [8] C. Huang, C. Zhang, S. Xiao, Y. Wang, Y. Fan, Y. Liu, N. Zhang, G. Qu, H. Ji, J. Han, L. Ge, Y. Kivshar, and Q. Song, *Science* **367**, 1018 (2020).
- [9] X. Gao, G. Zhao, M. Song, and X. Ao, *Nano Letters* **24**, 10943–10948 (2024).
- [10] B. Zhen, C. W. Hsu, L. Lu, A. D. Stone, and M. Soljačić, *Physical Review Letters* **113**, 257401 (2014).
- [11] H. M. Doeleman, F. Monticone, W. den Hollander, A. Alù, and A. F. Koenderink, *Nature Photonics* **12**, 397 (2018).
- [12] Y. Zhang, A. Chen, W. Liu, C. W. Hsu, B. Wang, F. Guan, X. Liu, L. Shi, L. Lu, and J. Zi, *Physical Review Letters* **120**, 186103 (2018).
- [13] J. Tian, G. Adamo, H. Liu, M. Wu, M. Klein, J. Deng, N. S. S. Ang, R. Paniagua-Domínguez, H. Liu, A. I. Kuznetsov, and C. Soci, *Advanced Materials* **35**, 10.1002/adma.202207430 (2022).
- [14] X. Yan, M. Tang, Z. Zhou, L. Ma, Y. Vaynzof, J. Yao, H. Dong, and Y. S. Zhao, *Nature Communications* **16**, 10.1038/s41467-025-57738-1 (2025).
- [15] X. Wu, S. Zhang, J. Song, X. Deng, W. Du, X. Zeng, Y. Zhang, Z. Zhang, Y. Chen, Y. Wang, C. Jiang, Y. Zhong, B. Wu, Z. Zhu, Y. Liang, Q. Zhang, Q. Xiong, and X. Liu, *Nature Communications* **15**, 10.1038/s41467-024-47669-8 (2024).
- [16] A. Aigner, T. Possmayer, T. Weber, A. A. Antonov, L. de S. Menezes, S. A. Maier, and A. Tittl, *Nature* **644**, 896–902 (2025).
- [17] V. A. Nguyen, H. S. Nguyen, Z. Yuan, D. X. Nguyen, C. Dang, S. T. Ha, X. Letartre, Q. Le-Van, and H. S. Nguyen, *Nanophotonics* **14**, 5229 (2025).
- [18] B. Bennett, R. Soref, and J. Del Alamo, *IEEE Journal of Quantum Electronics* **26**, 113–122 (1990).
- [19] S. W. Leonard, H. M. van Driel, J. Schilling, and R. B. Wehrspohn, *Physical Review B* **66**, 10.1103/physrevb.66.161102 (2002).
- [20] I. Fushman, E. Waks, D. Englund, N. Stoltz, P. Petroff, and J. Vučković, *Applied Physics Letters* **90**, 10.1063/1.2710080 (2007).
- [21] T. Ihn, *Envelope functions and effective mass approximation*, in *Semiconductor Nanostructures* (Oxford University Press, 2009) p. 53–62.
- [22] S. Zanotti, M. Minkov, D. Nigro, D. Gerace, S. Fan, and L. C. Andreani, *Computer Physics Communications* **304**, 109286 (2024).
- [23] T.-P. Vo, A. Rahmani, A. Belarouci, C. Seassal, D. Nedeljkovic, and S. Callard, *Opt. Express* **18**, 26879 (2010).
- [24] T.-P. Vo, M. Mivelle, S. Callard, A. Rahmani, F. Baida, D. Charraut, A. Belarouci, D. Nedeljkovic, C. Seassal, G. Burr, and T. Grosjean, *Opt. Express* **20**, 4124 (2012).
- [25] P. W. Atkins and R. S. Friedman, *Molecular Quantum Mechanics*, 5th ed. (Oxford University Press, 2011).
- [26] Y. Yu, E. Palushani, M. Heuck, D. Vukovic, C. Peucheret, K. Yvind, and J. Mork, *Applied Physics Letters* **105**, 10.1063/1.4893984 (2014).
- [27] M. R. Shcherbakov, S. Liu, V. V. Zubyuk, A. Vaskin, P. P. Vabishchevich, G. Keeler, T. Pertsch, T. V. Dogova, I. Staude, I. Brener, and A. A. Fedyanin, *Nature Communications* **8**, 10.1038/s41467-017-00019-3 (2017).
- [28] A. Aspuru-Guzik and P. Walther, *Nature Physics* **8**, 285–291 (2012).
- [29] T. Grass, D. Bercioux, U. Bhattacharya, M. Lewenstein, H. S. Nguyen, and C. Weitenberg, *Reviews of Modern Physics* **97**, 10.1103/revmodphys.97.011001 (2025).
- [30] Z. Chen, A. Sludds, R. Davis, I. Christen, L. Bernstein, L. Ateshian, T. Heuser, N. Heermeier, J. A. Lott, S. Reitzenstein, R. Hamerly, and D. Englund, *Nature Photonics* **17**, 723–730 (2023).
- [31] K. Ji, G. Tirabassi, C. Masoller, L. Ge, and A. M. Yacombotti, *Nature Communications* **16**, 10.1038/s41467-025-64252-x (2025).
- [32] S. Cuffeff, L. Berguiga, and H. S. Nguyen, *Nanophotonics* **13**, 841 (2024).

METHODS

Analytical model of the magnetic monopolar mode

Following the theoretical framework developed in Ref. [17], in this section we summarize the effective non-Hermitian model used to describe the magnetic monopolar mode of the honeycomb PhC slab. Near the Γ point, the Bloch field can be expressed as a coherent superposition of six TE-like guided modes $|n\rangle$ associated with the first-order reciprocal-lattice vectors $\mathbf{G}_{n=1..6}$,

$$\mathbf{G}_n = \frac{4\pi}{3a}(\cos \phi_n, \sin \phi_n)^T, \quad \phi_n = \frac{\pi}{3}(1 - n), \quad (\text{A1})$$

$$\hat{H}_\Gamma(\mathbf{k}) = \omega_\Gamma + \begin{pmatrix} v_\Gamma |\mathbf{k}_\parallel| \cos(\varphi - \frac{\pi}{3}) & V & W & U & W & V \\ V & v_\Gamma |\mathbf{k}_\parallel| \cos \varphi & V & W & U & W \\ W & V & v_\Gamma |\mathbf{k}_\parallel| \cos(\varphi + \frac{\pi}{3}) & V & W & U \\ U & W & V & -v_\Gamma |\mathbf{k}_\parallel| \cos(\varphi - \frac{\pi}{3}) & V & W \\ W & U & W & V & -v_\Gamma |\mathbf{k}_\parallel| \cos \varphi & V \\ V & W & U & W & V & -v_\Gamma |\mathbf{k}_\parallel| \cos(\varphi + \frac{\pi}{3}) \end{pmatrix} - i\gamma_0 \begin{pmatrix} 1 & \frac{1}{2} & -\frac{1}{2} & -1 & -\frac{1}{2} & \frac{1}{2} \\ \frac{1}{2} & 1 & \frac{1}{2} & -\frac{1}{2} & -1 & -\frac{1}{2} \\ -\frac{1}{2} & \frac{1}{2} & 1 & \frac{1}{2} & -\frac{1}{2} & -1 \\ -1 & -\frac{1}{2} & \frac{1}{2} & 1 & \frac{1}{2} & -\frac{1}{2} \\ -\frac{1}{2} & -1 & -\frac{1}{2} & \frac{1}{2} & 1 & \frac{1}{2} \\ \frac{1}{2} & -\frac{1}{2} & -1 & -\frac{1}{2} & \frac{1}{2} & 1 \end{pmatrix} \quad (\text{A2})$$

with $\varphi = \arg(\mathbf{k}_\parallel)$. Here the coupling strength U, V and W represent the diffractive couplings between the guided modes, while γ_0 represents the radiative coupling of the guided modes to free-space. All of these coupling strength are given by different Fourier components of the periodic dielectric function of the photonic crystal[17].

At $\mathbf{k}_\parallel = \mathbf{0}$, diagonalizing $\hat{H}(\mathbf{0})$ yields six eigenmodes. Because the honeycomb geometry satisfies $U < 0$, $V < 0$, and $W < 0$, the eigenvalue $\omega_0 = \omega_\Gamma + U + 2V + 2W$ correspond to the lowest mode at the Γ point. This mode does not radiate at normal incidence, and therefore, it constitutes a symmetry-protected BIC that forms the parent Bloch resonance for all trapped states studied in this work. Its eigenvector is $\mathbf{A}(\mathbf{0}) = (1, 1, 1, 1, 1, 1)^T$, up to normalization: the six first-order harmonics oscillate in phase. The other five modes (two dipolar, two quadrupolar, one hexapolar) are described in detail in Ref. [17].

Expanding the eigenvalue to second order,

$$\omega(\mathbf{k}_\parallel) \simeq \omega_0 + \underbrace{\frac{v_\Gamma^2 |\mathbf{k}_\parallel|^2}{2(2U + V + 3W)}}_{\alpha |\mathbf{k}_\parallel|^2} - i \underbrace{\gamma_0 \frac{3v_\Gamma^2 |\mathbf{k}_\parallel|^2}{2(2U + V + 3W)^2}}_{\gamma(\mathbf{k}_\parallel)} \quad (\text{A3})$$

reveals an isotropic parabolic dispersion. In our case $2U + V + 3W < 0$ (see Supplemental Materials), the effective

each carrying an in-plane polarization vector $\mathbf{p}_n = (-\sin \phi_n, \cos \phi_n)^T$. All six components correspond to the same fundamental TE guided mode of the effective homogeneous slab; the lattice simply couples these harmonics through diffraction and radiations. In this basis eigenmodes of the system is governed by an effective non-Hermitian Hamiltonian, given by:

mass $m = \hbar^2(2U + V + 3W)/v_\Gamma^2$ is negative.

To linear order in $|\mathbf{k}_\parallel|$, the eigenvector becomes

$$\mathbf{A}(\mathbf{k}_\parallel) \simeq \mathbf{A}(\mathbf{0}) + \frac{v_\Gamma |\mathbf{k}_\parallel|}{\sqrt{2}(2U + V + 3W)} \begin{pmatrix} \sin(\varphi + \frac{\pi}{6}) \\ \cos \varphi \\ -\sin(\varphi - \frac{\pi}{6}) \\ -\sin(\varphi + \frac{\pi}{6}) \\ -\cos \varphi \\ \sin(\varphi - \frac{\pi}{6}) \end{pmatrix}, \quad (\text{A4})$$

The electric field inside the slab (i.e. near field) follows

$$\mathbf{E}_{\text{near}}(\mathbf{r}_\parallel, z) = u(z) \sum_{n=1}^6 A_n(\mathbf{k}_\parallel) e^{i(\mathbf{G}_n + \mathbf{k}_\parallel) \cdot \mathbf{r}_\parallel} \mathbf{p}_n, \quad (\text{A5})$$

where $u(z)$ is the vertically guided mode profile. For the monopolar BIC at Γ , $A_n(\mathbf{0}) = 1$ for all n , giving

$$\mathbf{E}_{\text{near}}(\mathbf{r}_\parallel, z) \propto u(z) \sum_{n=1}^6 e^{i\mathbf{G}_n \cdot \mathbf{r}_\parallel} \mathbf{p}_n. \quad (\text{A6})$$

The magnetic field obtained from Maxwell's equations,

$$H_z(\mathbf{r}_\parallel, z) \propto u(z) \sum_{n=1}^6 e^{i\mathbf{G}_n \cdot \mathbf{r}_\parallel}, \quad (\text{A7})$$

produces a single-lobed, same-sign H_z distribution in each hexagonal unit cell, while the in-plane electric field $\mathbf{E}_{\text{near}}(\mathbf{r}_{\parallel}, z)$ forms a circulating pattern around the cell center. This fully symmetric A_1 texture — single-lobed H_z with circulating \mathbf{E}_{\parallel} is the origin of the term "magnetic monopolar".

The radiated field is the guided-mode superposition projected onto the outgoing channel via radiative coupling:

$$\mathbf{E}_{\text{far}}(\mathbf{k}_{\parallel}) \propto \sqrt{\gamma_0} \left[\sum_n A_n(\mathbf{k}_{\parallel}) \mathbf{p}_n \right]. \quad (\text{A8})$$

Using Eq. (A4) one obtains, to lowest order in $|\mathbf{k}_{\parallel}|$,

$$\mathbf{E}_{\text{far}}(\mathbf{k}_{\parallel}) \propto |\mathbf{k}_{\parallel}| \begin{pmatrix} -\sin \varphi \\ \cos \varphi \end{pmatrix} = |\mathbf{k}_{\parallel}| \hat{\mathbf{u}}_{\varphi}, \quad (\text{A9})$$

and therefore the monopolar mode is a BIC of topological charge +1 at Γ . Moreover, the radiative loss rate $\gamma(\mathbf{k}_{\parallel})$ can also be evaluated from the emitted intensity

$$|\mathbf{E}_{\text{far}}(\mathbf{k}_{\parallel})|^2 \propto \gamma_0 \frac{3v_{\Gamma}^2 |\mathbf{k}_{\parallel}|^2}{2(2U + V + 3W)^2}. \quad (\text{A10})$$

. This provides the same expression of $\gamma(\mathbf{k}_{\parallel})$ as the one obtained from the eigenvalue.

Far-field in real space of the trapped state

For a trapped state of envelope $F(\mathbf{r}_{\parallel})$ in real space, whose Fourier transform is $F(\mathbf{k}_{\parallel})$, the farfield in momentum space is given by $\mathbf{E}_{\text{far}}^{\text{trap}}(\mathbf{k}_{\parallel}) \propto \mathbf{E}_{\text{far}}(\mathbf{k}_{\parallel}) F(|\mathbf{k}_{\parallel}|)$. Moreover, from Eq. (A9), the radiation of the monopolar BIC near Γ scales as $\mathbf{E}_{\text{far}}(\mathbf{k}_{\parallel}) \propto |\mathbf{k}_{\parallel}| \hat{\mathbf{u}}_{\varphi} = \begin{pmatrix} -k_y \\ k_x \end{pmatrix}$, leading to

$$\mathbf{E}_{\text{far}}^{\text{trap}}(\mathbf{k}_{\parallel}) \propto F(|\mathbf{k}_{\parallel}|) \begin{pmatrix} -k_y \\ k_x \end{pmatrix}. \quad (\text{A11})$$

The real-space far-field distribution is obtained by inverse Fourier transform,

$$\mathbf{E}_{\text{far}}^{\text{trap}}(\mathbf{r}_{\parallel}) = \int F(|\mathbf{k}_{\parallel}|) \begin{pmatrix} -k_y \\ k_x \end{pmatrix} e^{i\mathbf{k}_{\parallel} \cdot \mathbf{r}_{\parallel}} dk_x dk_y. \quad (\text{A12})$$

Using the Fourier derivative identities $k_x e^{i\mathbf{k}_{\parallel} \cdot \mathbf{r}_{\parallel}} = -i \partial_x e^{i\mathbf{k}_{\parallel} \cdot \mathbf{r}_{\parallel}}$ and $k_y e^{i\mathbf{k}_{\parallel} \cdot \mathbf{r}_{\parallel}} = -i \partial_y e^{i\mathbf{k}_{\parallel} \cdot \mathbf{r}_{\parallel}}$, one obtains $\mathbf{E}_{\text{far}}(\mathbf{r}_{\parallel}) \propto \begin{pmatrix} -\partial_y F(\mathbf{r}_{\parallel}) \\ \partial_x F(\mathbf{r}_{\parallel}) \end{pmatrix}$. This can be written compactly as

$$\mathbf{E}_{\text{far}}^{\text{trap}}(\mathbf{r}_{\parallel}) \propto \hat{\mathbf{z}} \times \nabla F(\mathbf{r}_{\parallel}). \quad (\text{A13})$$

If the trapped-state envelope is radially symmetric, $F(\mathbf{r}_{\parallel}) = F(|\mathbf{r}_{\parallel}|)$, then $\nabla F = F'(|\mathbf{r}_{\parallel}|) \hat{\mathbf{u}}_r$. This yields an even simpler expression, given by $\mathbf{E}_{\text{far}}(\mathbf{r}_{\parallel}) \propto F'(|\mathbf{r}_{\parallel}|) \hat{\mathbf{u}}_{\varphi}$.

Therefore the real-space far-field corresponds to the azimuthal rotation of the gradient of the envelope function. For any radially symmetric trapped state, the emission vanishes at the center and forms a ring-shaped intensity profile determined by the radial derivative of the envelope.

Determination of the potential amplitude V_0

The envelope function and the corresponding eigenenergy of the trapped state are obtained by numerically solving the two-dimensional Schrödinger equation $-\frac{\hbar^2}{2m} \nabla_{\mathbf{r}_{\parallel}}^2 F(\mathbf{r}_{\parallel}) + V(\mathbf{r}_{\parallel}) F(\mathbf{r}_{\parallel}) = E F(\mathbf{r}_{\parallel})$, where $F(\mathbf{r}_{\parallel})$ denotes the envelope function, $V(\mathbf{r}_{\parallel})$ the effective potential induced by the pump, and E the corresponding eigenenergy.

For single-spot pumping, the carrier-induced potential is modeled as a Gaussian profile $V(\mathbf{r}_{\parallel}) = V_0 \exp\left(-\frac{|\mathbf{r}_{\parallel}|^2}{\sigma^2}\right)$, characterized by the pump waist σ and the potential amplitude V_0 . The waist σ is determined experimentally from a Gaussian fit to the real-space pump-intensity profile on the sample. The potential amplitude V_0 is then treated as a fitting parameter and adjusted until the eigenenergy obtained from the Schrödinger solver reproduces the confinement energy ΔE measured experimentally in the saturated regime [Fig. 3(d)].

Experimental setup for farfield measurements

Energy–momentum dispersions were measured using a custom-built back-focal-plane (BFP) imaging setup. The Fourier plane of a $\times 100$ microscope objective (NA = 0.8) was imaged onto the entrance slit of a grating spectrometer (HRS-500MS-NI, Princeton Instruments). The sample was mounted such that its x -axis, corresponding to the Γ – K direction of the honeycomb lattice, was aligned with the slit. The spectrum dispersed by the grating was detected using a two-dimensional InGaAs camera (Nirvana HS, Princeton Instruments), providing simultaneous access to k_x and optical energy. To measure the Γ – M dispersion, the sample was rotated such that its y -axis aligned with the slit, providing access to k_y . Angle-resolved reflectivity [Fig. 2(d)] and angle-resolved photoluminescence [Figs. 3(b) and 5(b)] are acquired using the same setup but with different illumination sources: a broadband halogen lamp for reflectivity and a femtosecond laser (800nm, Coherent Chameleon Ultra II) for photoluminescence.

Real-space and momentum-space far-field intensity and polarization maps [Figs. 2(e-g), 4(d-g), and A1] are obtained on the same optical platform operated in a tomographic configuration, in which either the BFP plane or the object plane was scanned relative to the spec-

trometer slit while selecting different polarization analyzers. This method, which yields quantitative polarization-resolved images in both (k_x, k_y) and (x, y) , is described

in detail in our previous study [32]. For a detailed description of the optical setup refer to the Supplementary Material.

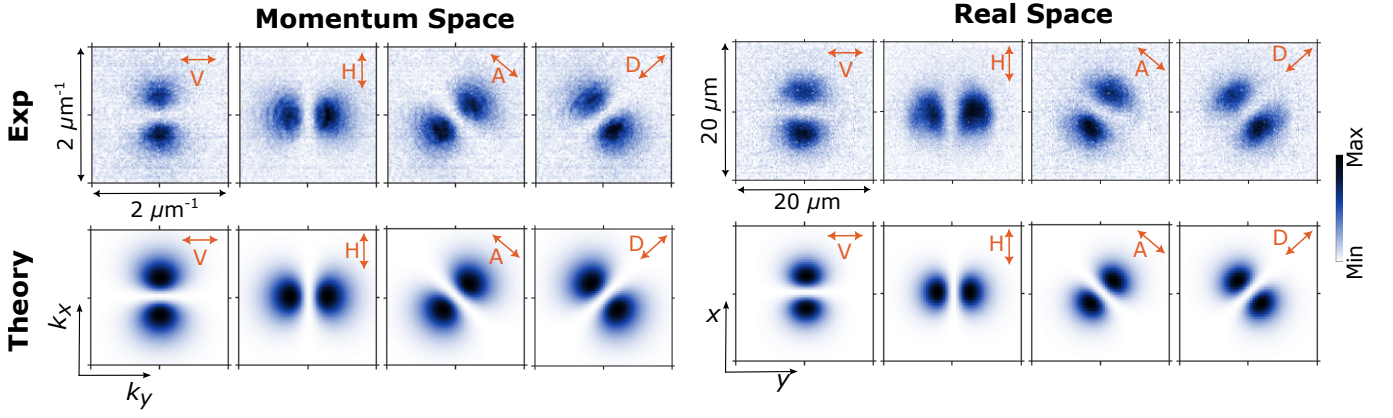


Figure A1. **Polarization-resolved maps under single-spot pumping.** Experimental and theoretical polarization-resolved far-field lasing images in both real and momentum space for a pump waist $\sigma = 3.2 \mu\text{m}$. A linear polarizer is placed in front of the InGaAs camera (see Methods) and rotated to 0° (H), 45° (D), 90° (V), and 135° (A). For comparison, polarization-integrated images without a polarizer are shown in Fig. 3(e-h).

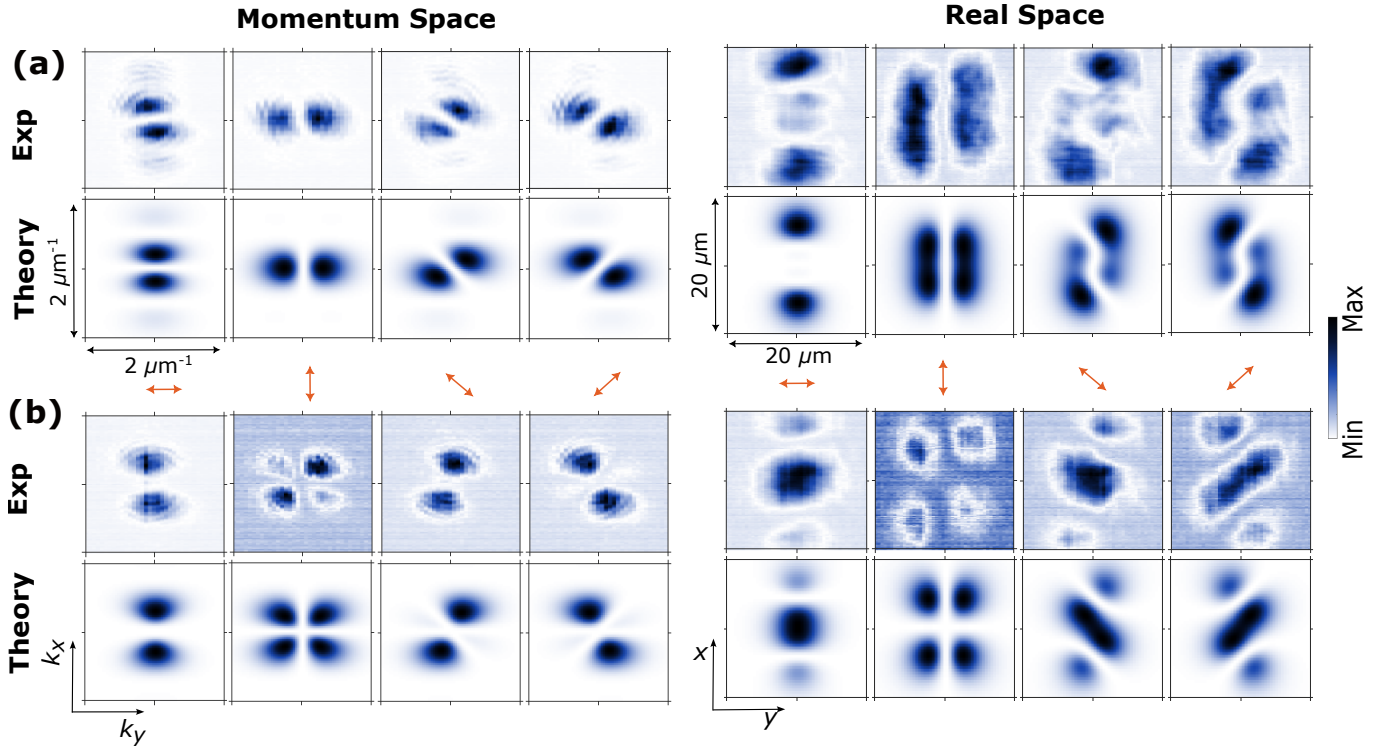


Figure A2. **Polarization maps for double-spot pumping.** Polarization-resolved far-field lasing images for the (a) bonding and (b) antibonding modes in real and momentum space, corresponding to the data shown in Fig. 5(d-g). A linear polarizer placed in front of the detector is rotated to 0° , 45° , 90° , and 135° . The top and bottom rows display the experimental and analytical results, respectively.

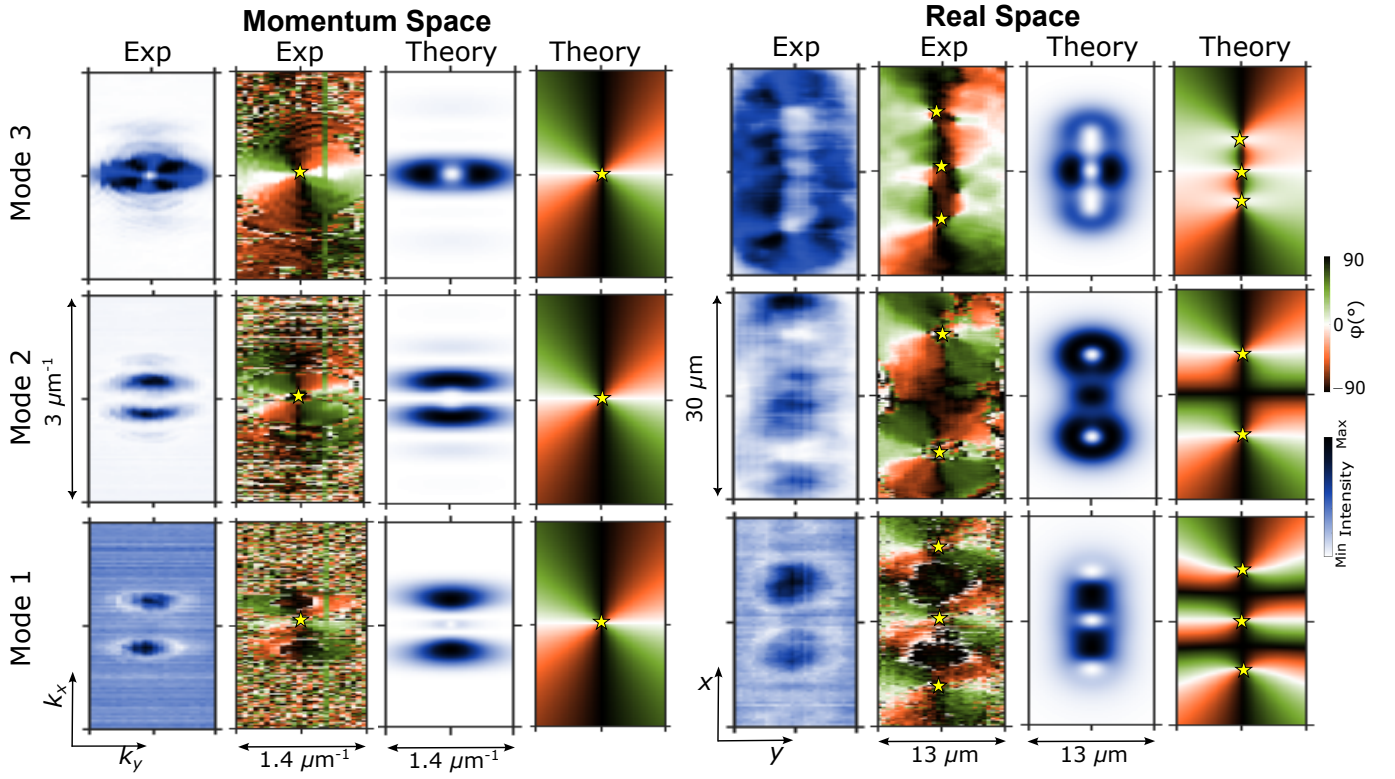


Figure A3. **Three-spot pumping and multi-singularity trapped modes.** Experimental and theoretical far-field characterization of the three trapped modes formed under three-spot pumping with spot separation $L = 13 \mu\text{m}$ and spot size $\sigma = 2.5 \mu\text{m}$. Each row corresponds to one of the three trapped eigenstates supported by the triple-well potential. For each mode, the panels show (from left to right): experimental real-space intensity, experimental real-space polarization texture, theoretical real-space intensity, theoretical real-space polarization texture. The same sequence is used for the momentum-space emission. The number and spatial arrangement of real-space polarization singularities (yellow stars) directly follow from the nodal structure of the pump-induced envelope function: one singularity for the ground state (Mode 1), two for the first excited state (Mode 2), and three for the second excited state (Mode 3). In contrast, all modes preserve the same momentum-space vortex at Γ , inherited from the monopolar BIC of the underlying Bloch resonance.

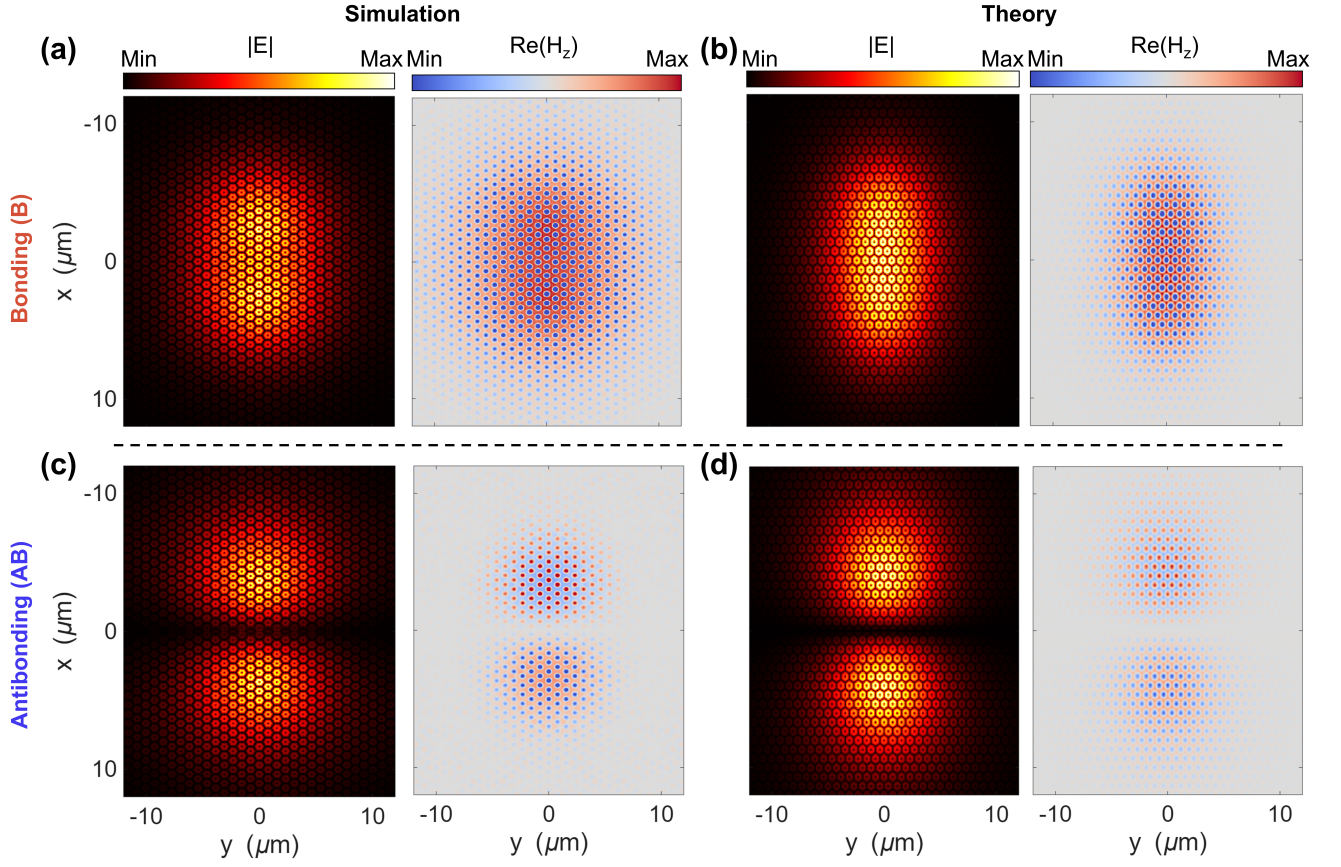


Figure A4. Near-field map of the trapped states under the coupled Gaussian pumps $V(x, y) = V_0 \left[e^{-((x-L/2)^2 - y^2)/\sigma^2} + e^{-((x+L/2)^2 + y^2)/\sigma^2} \right]$. The symmetric and antisymmetric against $x = 0$ exhibit the feature of bonding and antibonding mode.

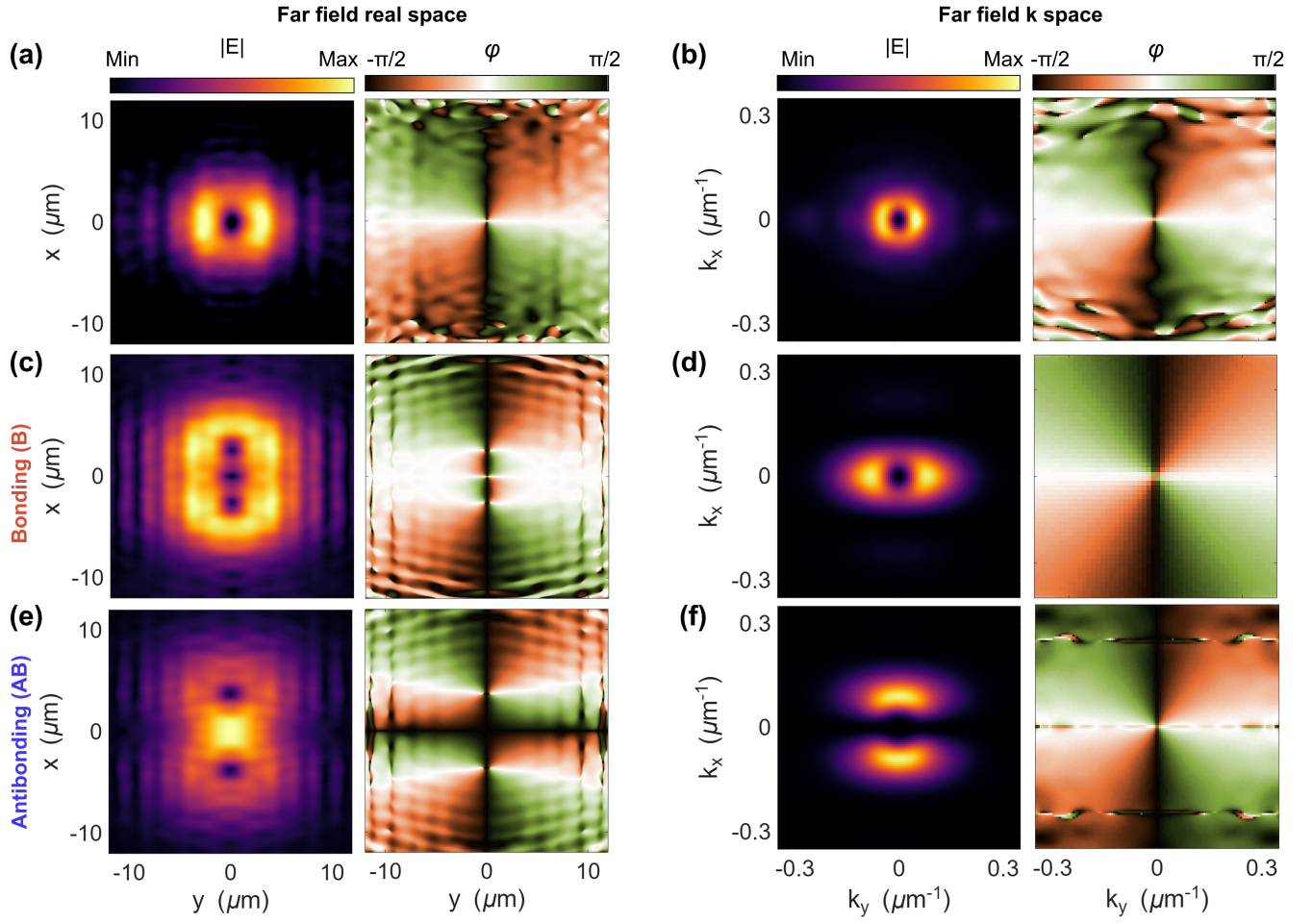


Figure A5. Numerical simulation results of far-field patterns and polarization angles in real and momentum space. **(a-b)** Single barrier with $\sigma = 3.2\mu\text{m}$. **(c-f)** Bonding and Antibonding modes from double barriers with $\sigma = 4\mu\text{m}$ and $L = 8\mu\text{m}$.